



# Long-distance distributed pressure sensing based on frequency-scanned phase-sensitive optical time-domain reflectometry

LI ZHANG,<sup>1,\*</sup>  ZHISHENG YANG,<sup>1,2</sup>  ŁUKASZ SZOSTKIEWICZ,<sup>3,4</sup>   
KRZYSZTOF MARKIEWICZ,<sup>3</sup>  SERGEI MIKHAILOV,<sup>5</sup> THOMAS  
GEERNAERT,<sup>5</sup> ETIENNE ROCHAT,<sup>6</sup> AND LUC THÉVENAZ<sup>1</sup> 

<sup>1</sup>Group for Fibre Optics, Ecole polytechnique fédérale de Lausanne (EPFL), SCI-STI-LT Station 11, 1015 Lausanne, Switzerland

<sup>2</sup>Present address: State Key Laboratory of Information Photonics & Optical Communications, Beijing University of Posts and Telecommunications, Beijing 100876, China

<sup>3</sup>InPhoTech sp. z o.o. ul. Poznańska 400 05-850 Otarzew, Poland

<sup>4</sup>Faculty of Physics, Warsaw University of Technology, Warsaw 00-662, Poland

<sup>5</sup>Department of Applied Physics and Photonics, Vrije Universiteit Brussel, Brussels B-1050, Belgium

<sup>6</sup>Omnisens SA, 3 Riond Bosson, 1110 Morges, Switzerland

\*li.zhang@epfl.ch

**Abstract:** In this paper, a long-distance distributed pressure sensing system based on a special fiber and using frequency-scanned phase-sensitive optical time-domain reflectometry is proposed. The fiber shows high pressure sensitivity (159 MHz/bar) and low loss (3 dB/km) owing to its simple structure made of two large air holes in the cladding. The pressure response of the two orthogonal polarization axes of the fiber is explored distinctively. Distributed pressure sensing over a long sensing range (720 m) and high spatial resolution (5 cm) is demonstrated, resulting in 14,400 resolved sensing points with uncertainty on pressure of 0.49 bar. Discrimination between the temperature/strain and pressure responses is demonstrated, taking advantage of the different pressure and temperature sensitivities of the two polarization axes. In addition, the temperature response of the fiber is studied and the simulation results show the possibility of scaling the temperature sensitivity by adjusting the size of the core. The sensing distance limit due to crosstalk between the polarization axes is also discussed.

© 2021 Optical Society of America under the terms of the [OSA Open Access Publishing Agreement](#)

## 1. Introduction

Distributed fiber sensing (DFS) has drawn much attention since it provides a cost effective solution by sensing information from thousands of or even millions of locations using just one interrogator and a single fiber, instead of deploying a complex sensor array. Great efforts have been devoted in the past few decades to improve the sensing range, spatial resolution, the number of spatially-resolved points, dynamic range, response bandwidth, etc [1–4]. Traditional DFSs using standard single mode fibers (SMF) are mostly focused on temperature and axial strain sensing. However, with proper designs of the fiber, different quantities (such as chemical detection, radiation and humidity), indirectly inducing a temperature or strain change in the fiber, have been explored recently [5–7]. The progresses on DFSs bring key contributions for many applications in various domains such as structural health monitoring, security surveillance, oil, gas and other energy industry [8–10].

Pressure sensing is also of important significance in the domains mentioned above; moreover, pressure monitoring of multiple locations is subject to a high demand from today's complex industrial facilities and systems [11]. A few distributed pressure sensing (DPS) schemes have been proposed based on Brillouin scattering using fibers with special coatings [12–14], dynamic

gratings [15,16] or optical frequency-domain reflectometry (OFDR) [17–19], demonstrating the great potential of DPS using DFS technology. However, either the pressure sensitivity is relatively low due to the large Young's modulus of the fiber material silica [12–16], or the sensing range is fundamentally limited by the sensing range of OFDR [17–19].

In 2019, a DPS system based on phase-sensitive optical time-domain reflectometry ( $\Phi$ -OTDR) was proposed using a birefringent photonic crystal fibers (PCFs), which showed a high pressure sensitivity at sharp spatial resolution (5 cm) [20]. However, the PCFs in [20] show a birefringence with large fluctuations and a high loss due to the complex structure of the fibers, which limits the sensing range to a few tens of meters. The potential to cover a larger distance is nevertheless present, since that small spatial resolution was previously demonstrated for temperature sensing using a single mode fiber over a sensing distance in the kilometer range based on a similar interrogating scheme [21]. Therefore, a more specific fiber design is needed to fulfill the requirement for practical long-distance pressure sensing, minimizing the amplitude of birefringence fluctuations while massively reducing the propagation loss.

In this paper, a DPS system is proposed based on  $\Phi$ -OTDR with frequency scanning using an elliptical core fiber with side air holes (SAHF) in the cladding, based on the measurement of its birefringence change when pressure is applied. Thanks to the large air holes in the cladding, the fiber shows a high pressure sensitivity of 159 MHz/bar. Compared with the PCF in [20], the smartly designed SAHF shows a much simpler structure, leading to a massive loss reduction (3 dB/km), which is essential for long distance distributed sensing, while maintaining a comparable pressure sensitivity. As a result, pressure sensing with 5 cm spatial resolution and 720 m sensing range is demonstrated, leading to 14,400 resolved sensing points subject to a pressure uncertainty of 0.49 bar. The additional benefit of a low temperature sensitivity of the birefringence (6 MHz/k) is verified experimentally, too. Incidentally, a full discrimination between temperature/strain and pressure responses is demonstrated for the first time in distributed fiber sensing, taking advantage of the different pressure and temperature sensitivities for the light propagating along either of the two orthogonal polarization eigenaxes. In addition, pressure and temperature sensitivities for different core diameters are investigated through simulation. The results show a trade-off between the temperature sensitivity and the fiber loss, which can be adapted by adjusting the ellipticity of the core. We also discuss the sensing distance limit due to the crosstalk between the two polarization principal axes.

## 2. Principle

The working principle of the proposed DPS is illustrated in Fig. 1: the birefringence change of the fiber caused by the pressure change can be retrieved by comparing the frequency shift in Rayleigh spectra of the two polarization axes, respectively. The Rayleigh scattering (RS) spectrum of all the sensing locations along the fiber can be obtained by simply scanning the frequency of the interrogating optical pulses. The local phase change of the fiber, induced by environmental changes, such as temperature, strain or hereby pressure variations, can be retrieved from the frequency shift (FS) of the corresponding RS spectrum with respect to a reference RS spectrum [22]. For a birefringent fiber, since the refractive indices of the two polarization principal axes are different, the RS spectra also depend on the polarization of the interrogating pulses. By sending optical pulses with orthogonal polarizations, aligned sequentially along the two principal polarization axes of the fiber, respectively, and then scanning the frequency of the interrogating light pulse, the system enables to interrogate the RS spectra of the two axes separately. Since the structure of the fiber is asymmetric, the pressure-induced phase changes for each polarization axis are different, i.e. the birefringence change can be evaluated from the difference in the FSs of each axis.

In 1986, optical fibers known as side air-hole fibers (SAHF) were specifically designed to achieve pressure sensing [23]. The two large air holes in their cladding bring a strong asymmetry

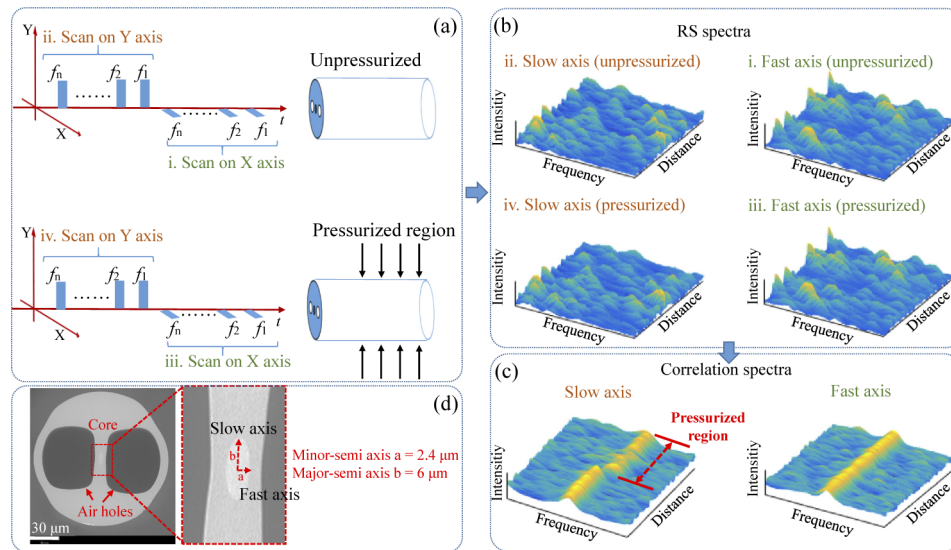


**Fig. 1.** Pressure sensing principle: (a) frequency scanning sequence for the interrogating pulses of the reference and live measurements; (b) corresponding coherent Rayleigh scattering (RS) spectral and distance map; (c) correlation spectra between reference and live measurements for each polarization axis; (d) SEM image of the sensing fiber cross section

in the fiber cross-section, with the direct purpose that a variation of the external pressure will induce changes in the fiber birefringence. The sensitivity of SAHF to pressure is high since the volume occupied by the air holes as well as the asymmetry of the fiber cross section is large [24]. The fiber structure resembles the PM "panda" fiber, except that the fiber core is here surrounded by two large air holes instead of stress-applying rods in "panda" fibers. The two remarkable features of this SAHF fiber are the simplicity of its structure and its core dimension similar to SMFs. These features translate into a low propagation loss together with a reasonable splicing loss, making SAHFs promising candidates for long distance distributed fiber sensing. The fiber we used here is a specially designed fiber manufactured by InPhoTech, showing an elliptical core and two large air side holes in the cladding. Its cross-section is shown in Fig. 1(d), with lengths of the minor and major semi-axes of  $2.4 \mu\text{m}$  and  $6 \mu\text{m}$ , respectively. It maintains the key features of SAHFs of a low propagation loss (3 dB/km) and a low splicing loss (less than 1 dB). In addition, the elliptical core increases the birefringence of the fiber, significantly alleviating any polarization cross talk. However, the temperature sensitivity turns out to be slightly increased, too, and this will be explained more in details in the discussion section.

Owing to the large air holes in the cladding of the SAHF, the stress induced by the pressure loading on the fiber concentrates more on the Y axis (slow axis), resulting in a significant enhancement of the pressure sensitivity on this axis, while the pressure sensitivity on the X axis (fast axis) is kept similar to that of a plain solid SMF. Therefore, the optical path change on the Y axis (or slow axis) will be much larger than on the X axis (or fast axis) under the same pressure change condition, resulting in a large frequency shift for the Y axis while the other axis experiences a minor effect, as shown in Fig. 1(c).

### 3. Experimental setup

The experimental setup is sketched in Fig. 2, where the interrogator is the same as in [20,25]. The light source consists of a distributed feedback laser (DFB) with a linewidth of 1 MHz, followed by an intensity modulator (two cascaded electro-optic modulators) and an erbium-doped fiber

optical amplifier (EDFA) to shape optical pulses with high enough extinction ratio and short pulse duration. The optical pulses are then sent to a polarization switch and controller, so that their polarization states can be alternatively aligned along each polarization eigenaxis of the fiber under test. The frequency shift (FS) induced by a temperature change  $\delta T$  or a pressure change  $\delta P$  can be evaluated separately along each axis by performing a cross correlation on their RS spectra separately.

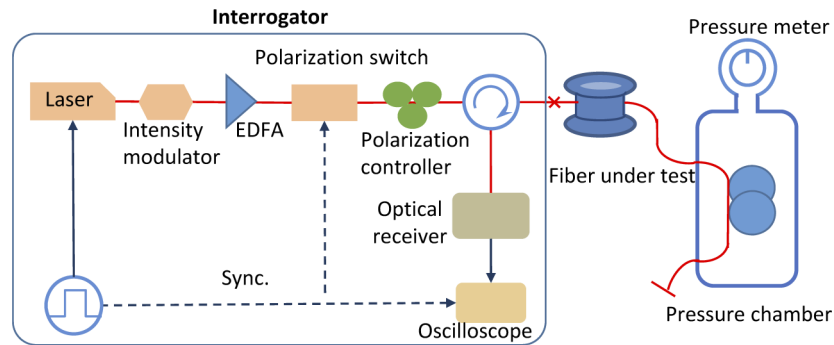


**Fig. 2.** Experimental setup.

Fast and broad (50 GHz) frequency scans of the interrogating pulses are achieved by direct tuning of the laser current with a frequency scanning step of 81 MHz, where the laser has been calibrated before the measurement using an optical spectral analyzer with a high resolution of 4 MHz, so that the dependence of the laser frequency on the injected current is precisely determined. The laser is classically temperature-controlled by a dedicated driver, so that the frequency shift drift can be ignored over a relatively short time. A segment of about 5 m long near the fiber end is placed into a hydro-static oil pressure chamber monitored by a pressure meter based on an electric transducer. The SAHF under test shows a birefringence of  $\sim 5 \times 10^{-5}$  in term of refractive index. The length of the fiber under test is  $\sim 720$  m.

## 4. Experimental results

### 4.1. Pressure and temperature sensitivities

A first test has been carried out when the fiber is interrogated using a 2 ns pulse, corresponding to a spatial resolution of 20 cm. The pressure-induced frequency shifts for the two orthogonal polarizations are measured from 0 to 18 bar and results are shown in Fig. 3(a). The sensitivities for the two axes are calculated to be 148.6 MHz/bar and -10.4 MHz/bar, respectively. A discrepancy can be observed between these numbers and those published in [25], though they concern the same fiber (Fiber H in [25]). However, the pressure test bench we used before was a gas chamber that only sustains a maximum pressure of 2 bar. Only 4 distinct pressure values could be applied over this much restricted range. Besides, the chamber experienced substantial temperature changes when varying the chamber pressure as a result of the gas compression-decompression processes. In the experiment reported here, a pressurizing liquid (oil) is used. It can sustain much higher pressures and the temperature tends to be constant during the pressure change process. Altogether this significantly increases the reliability of the result presented here.

We also tested the temperature sensitivity of the birefringence by placing a section of the SAHF into a thermal water bath and monitoring the water temperature precisely with a Platinum resistance thermometer. From the results shown in Fig. 3(b) we can see that the thermal responses on both axes are nearly the same, confirming the results obtained in side hole fibers with Bragg

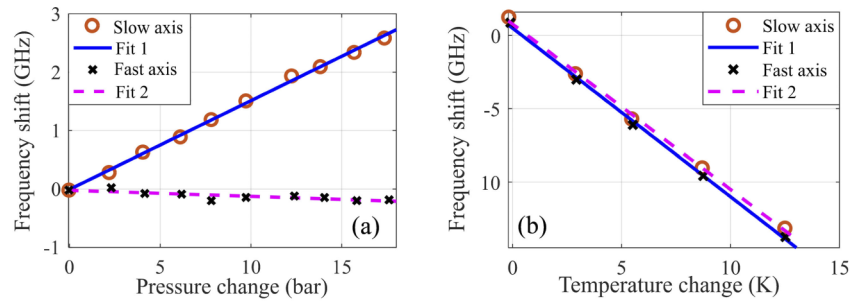


**Fig. 3.** (a) Pressure and (b) temperature responses of the two polarization principal axes of the fiber.

gratings (FBG) imprinted in the fiber core [26]. The temperature sensitivities are -1.121 GHz/K and -1.116 GHz/K for the fast axis and slow axis, respectively.

The birefringence response to temperature, calculated from the experimental results, is 6 MHz/K, which is much smaller compared to the expected changes of pressure in field conditions, since 1 K change gives an equivalent shift to that caused by a pressure change of 0.04 bar, considering the pressure response of 159 MHz/bar. This comes from a birefringence dependence on temperature mainly due to a differential thermal expansion between cladding and core of the fiber for fast and slow axes, which remains limited with this fiber design. The pure temperature dependence of the refractive index (thermo-optical effect) can be reasonably considered as identical for the 2 axes.

#### 4.2. Long-distance distributed pressure sensing with high spatial resolution

After the characterizations of the fiber sensitivities, we reduced the pulse width to 500 ps (i.e. 5 cm spatial resolution) to bring the system to its ultimate performance. The pressure responses of the correlation spectra of both polarization axes under a pressure change of 12 bar are illustrated in Fig. 4, from which we can see a clear frequency shift for the slow axis (in Fig. 4(a)) but no marked frequency shift for the fast axis in Fig. 4(b). In Fig. 5, the pressure change distribution along the fiber is calculated through the pressure sensitivity obtained in the previous section. The results matches well with the applied pressure (12 bar) and the high spatial resolution is confirmed from the step transition shown on the magnified section in Fig. 5(b).

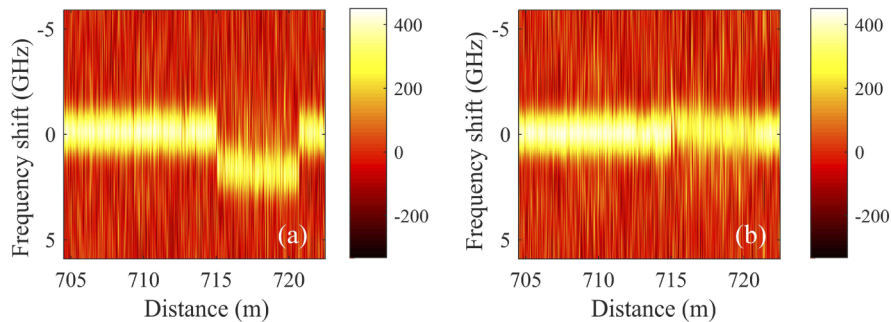


**Fig. 4.** Correlations of RS spectra when a 12 bar pressure is applied. (a) slow axis; (b) fast axis (5 cm spatial resolution). Only a section containing the pressure chamber and some spare pressure-free lengths is represented, located near the fiber far end.

The calculated pressure uncertainty is estimated to be 0.49 bar, by dividing the measured frequency uncertainty  $\Delta F$  by the measured pressure sensitivity  $S_P$ , i.e.  $\Delta P = \Delta F / S_P$ , where

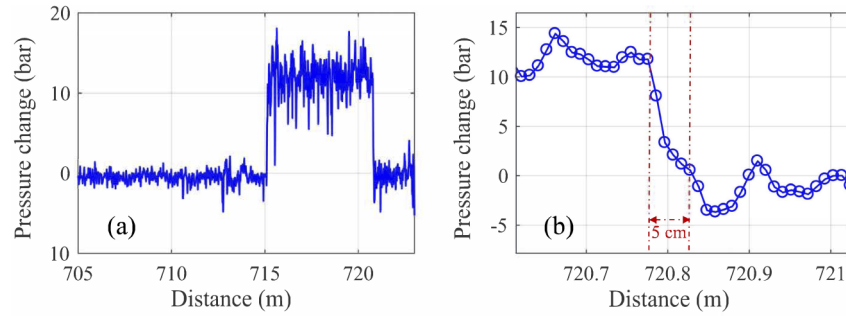


**Fig. 5.** (a) Pressure change distribution along the final section of the fiber where pressure is applied; (b) Magnified view around the position of a pressure step transition (chamber outlet), demonstrating the 5 cm spatial resolution.

$\Delta F$  is the estimated standard deviation over the first 100 points of the measured frequency shift. Ideally the pressure experienced by the fiber in the chamber should be uniform, provided that the fiber is fully surrounded by the liquid. However, in some locations, the fiber may be touching the pipe wall, so that the pressure is here not isotropic any more. This might be the reason why the measured pressure in the chamber shows larger fluctuations. The fiber before the pressure chamber has been placed into a water bath to be isolated from environmental fluctuations, while the small portion after the chamber could not be. This simply explains why the fluctuations after the pipe are also more pronounced.

It should be noted that the pressure change applied to the fiber does not exceed 15 bar, as a result of spurious leaks around fiber by-passes at high pressure. Actually, the measurable range is only limited by the reference frequency range of the laser scan. Since the hydrostatic pressure measurement does not require a fast measurement, the scan can be achieved by tuning the laser temperature, and normally this can enable a scanning range of some 200 GHz for a DFB laser. As reported in [21], a temperature range larger than 100 °C can be measured using a very similar system, which translates into an equivalent pressure change of some 1000 bar.

#### 4.3. Pressure and temperature discrimination

In Fig. 3, the measured frequency shifts on both polarization axes are represented when temperature and pressure changes are distinctively applied, indicating a clear potential to discriminate the two quantities. While the frequency shifts due to temperature are basically identical for the 2 birefringence axes, they are clearly distinct in the case of pressure, so that it leads to a well-conditioned set of 2 equations connecting frequency shifts from the 2 axes and the 2 quantities under question. Similar to the approach in [27], the frequency shifts of the system can be described as follows:

$$\begin{bmatrix} \delta F_{fast} \\ \delta F_{slow} \end{bmatrix} = \begin{bmatrix} S_{T,fast} & S_{T,slow} \\ S_{P,fast} & S_{P,slow} \end{bmatrix} \times \begin{bmatrix} \delta T \\ \delta P \end{bmatrix} \quad (1)$$

where  $\delta T$ ,  $\delta P$  and  $\delta F$  are the temperature change, pressure change and the frequency shift of the system, respectively. The subscript of  $\delta F$  designates the polarization axis.  $S_{i,j}$  is the sensitivity where  $i$  represents the temperature (T) and pressure (P) and  $j$  represents the polarization axis. The obtained experimental values for these sensitivities are given in section 4.1.

A demonstration of the discrimination between pressure and temperature/strain has been carried out and the results are shown in Fig. 6. The length of the fiber under test is 8 m and the first 3 m is placed into a water bath to keep the temperature constant, and the last 2 m (6-8 m) fiber is inserted into the pressure chamber to be subject to pressure changes. There is 3 m of

fiber in-between exposed to air and subject to the changes of the ambient temperature. Different pressure changes (3 bar, 6 bar and 9 bar) are applied to the fiber and the frequency shift responses on both polarization axes are depicted in Fig. 6(a) and (b). It can be observed that frequency shifts take place not only in the pressure chamber, but also over the air-exposed segment. By inverting the well-conditioned matrix in Eq. (1), both the pressure and temperature changes can be extracted, which are represented in Fig. 6(c) and (d). The retrieved pressure changes match the actual applied pressures and it can be observed that there is a raise of the ambient temperature while the experiment was carried out, as monitored by the segment exposed to air between the water bath and the pressure chamber. From the experimental data, the accuracy on temperature and pressure is calculated to be  $0.014\text{ }^{\circ}\text{C}$  and  $0.15\text{ bar}$ , respectively, using the estimated standard deviation over the first 100 points. The pressure accuracy is better than the  $0.49\text{ bar}$  in Section 4.2 because the fiber is here much shorter.

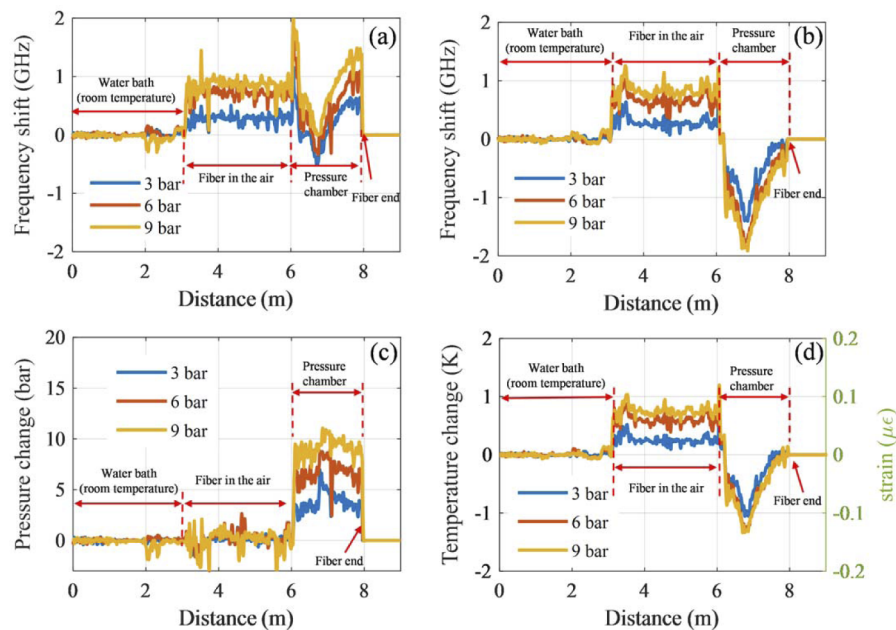


**Fig. 6.** Responses of (a) fast and (b) slow axis when 3 bar, 6 bar and 9 bar pressure changes are applied to the fiber. From these responses and after inverting Eq. (1) the following distributions for physical quantities are obtained: (c) pressure and (d) temperature/strain

It should be noted that the pressure fluctuations in Fig. 6(c) can be divided into 2 categories: the first type of fluctuations is due to the anisotropic pressure experienced by the fiber, as addressed in the previous sub-section. It is an implementation problem of the pressure test bench rather than an issue related to the interrogator or the sensing fiber, which can be avoided with an upgraded pressure test bench. A second type of fluctuations, which is more fundamental, results from the nonuniform strain and temperature applied on the fiber. As shown in Fig. 6(d), the strain along the fiber in the chamber is not uniform, and the pressure fluctuations in Fig. 6(c) are obviously correlated with the strain profiles. Although the strain and temperature can be discriminated from the pressure change, they still induce correlated errors and uncertainties in the pressure determination. For instance the traces variations in the pressure chamber in Fig. 6(d) are believed to result from an applied strain caused by a length expansion of the chamber pipe when pressure is applied. The strain profile along the pipe clearly supports this possible explanation.

## 5. Discussions

### 5.1. Temperature and pressure cross-sensitivity

An important issue for DPS remains the cross-sensitivity between temperature/axial strain and pressure (transverse strain). Although the experimental results show that the temperature sensitivity of the fiber is fairly reduced when compared to its pressure sensitivity, it may be worth investigating if the temperature sensitivity can be further reduced.

The main contributions to the optical path change induced by temperature along the fiber are: first, the difference between the thermal expansion coefficients in the cladding and the core of the fiber; second, the temperature-induced change in the refractive index of the fiber [28]. The tested SAHF contains two air holes in the cladding, impacting the birefringence through a differential thermal expansion; in addition, the elliptical core shape of the fiber impacts the temperature dependence of birefringence, too, through a thermally-induced differential change on the effective refractive index of the two polarization modes. These 2 effects may induce opposite changes under given conditions. It means that, with a proper design on the fiber structure, the temperature sensitivity of birefringence can be reduced and in principle even completely canceled out.

As for the dependency of the pressure sensitivity on the fiber geometry, it has been demonstrated that the pressure sensitivity is linearly proportional to  $\gamma^2$ , where  $\gamma$  is the angle between the line connecting the core and air hole centers and the tangent to the air hole passing by the fiber center, as shown in Fig. 7 (the air holes are assumed to be circular for simplicity) [24]. As a consequence, the variation of the core ellipticity has in principle no impact on the pressure sensitivity, under the condition that the core is much more smaller than the air holes.

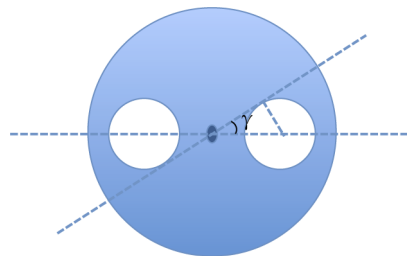


**Fig. 7.** The pressure sensitivity depends quadratically on the angle  $\gamma$

To verify this concept, we performed simulations using Comsol, by varying the length of the major semi-axis  $b$  of the elliptical core, to predict the pressure and temperature sensitivities of the fiber birefringence. The simulation results are shown in Fig. 8 as blue lines and the experimental values from our only tested fiber are represented as orange dots.

As illustrated in Fig. 8(a), on one hand the temperature sensitivity drops significantly, as  $b$  decreases or even turns shorter than the minor semi-axis  $a$ , to reach a value of 1.05 MHz/K when  $b = 2 \mu\text{m}$ . This is 5 times smaller than for the tested SAHF. This definitely suggests that an orientation of the core ellipse orthogonal to the situation of the tested SAHF (see Fig. 1) will lead to a significant decrease or even a vanishing of the temperature dependence of the birefringence. In this case the longer axis of the ellipse will be oriented perpendicular to the narrow glass wall between the air holes and this orientation may cause challenging fabrication issues.

On the other hand, the pressure sensitivity doesn't change much with the decrease of  $b$ . The experimental values of the fiber we used are shown in the figure, showing a good agreement with the simulations. It must be mentioned that zero temperature sensitivity is not specific to this type of fibers and can be obtained in birefringent photonic crystal fibers [29].

Nevertheless there exists a trade-off between the temperature sensitivity and the fiber loss. As the core area turns smaller, the optical field will be less confined in the core and the loss due to

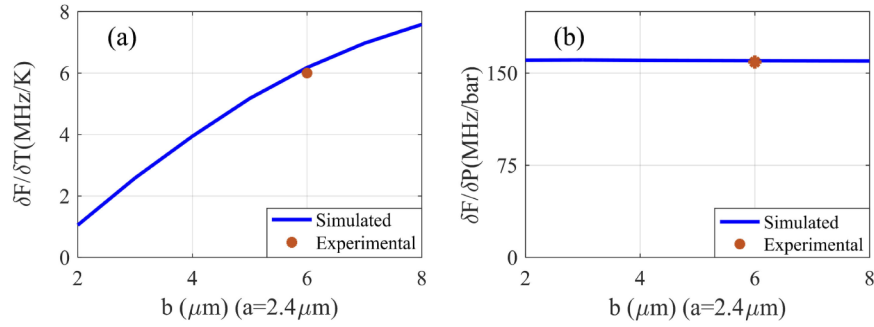


**Fig. 8.** (a) Temperature and (b) pressure sensitivities with different core ellipticities (a, b: semi-axis length).  $\delta F$  is obtained by subtracting the responses from the slow axis to the fast axis, which describes the birefringence change of the fiber. Parameters used for simulation: 72 GPa, 0.17,  $1.14 \times 10^{-6}$  [1/K], and  $5.5 \times 10^{-7}$  [1/K] for Young's modulus, Poisson ratio and thermal expansion coefficient for core and cladding, respectively.

surface scattering on the air hole interface will increase and therefore limit the sensing range. The essential merit of SAHF is to offer an excellent combination of a high response to pressure and a moderately low temperature sensitivity with a small loss, which is essential for long range distributed pressure sensing.

## 5.2. Polarization crosstalk

Since the pressure sensitivities on the two polarization axes are different, the accumulated crosstalk between polarizations contaminates and distorts the coherent Rayleigh response when a pressure change is applied to the fiber, hence limiting the sensing distance range of the system. It is therefore essential to address the polarization crosstalk in the context of this study.

The polarization mode-coupling is due to waveguide fluctuations and anisotropic Rayleigh scattering [30], and the strength of the polarization coupling can be characterized by the mode-coupling parameter:

$$h(\beta) = \frac{2\langle \hat{\Gamma} \rangle^2 l}{[1 + (\Delta\beta)l]^2} \quad (2)$$

where  $\Delta\beta = |\beta_x - \beta_y|$  and  $\beta_x, \beta_y$  are the propagation constants for the two principle polarization axes.  $l$  is the correlation length of the fluctuations and  $\hat{\Gamma}$  is an auxiliary constant to allow expressing the local coupling coefficient as  $\Gamma_{xy}(z) = \hat{\Gamma}f(z)$ , where  $f(z)$  represents the fluctuation of the waveguide parameters.

For highly birefringent fibers, only the polarization coupling due to waveguide fluctuations is taken into consideration, since its correlation length (in the order of  $10^{-2}$  m) is much larger than that of Rayleigh scattering (much shorter than  $10^{-6}$  m). From the knowledge obtained by studying Panda fibers, the mode coupling mainly originates from the deformations of stress-applying parts [31]. By similarity, we here assume that the deformations of the side holes is the main origin for mode coupling, justified by the structural resemblance of the 2 types of fiber. Then we use the approximation [31]:

$$\hat{\Gamma} = -\frac{2}{7}k(C_1 - C_2)(0.108 - \Delta)\hat{\theta}_d \text{ (m}^{-1}\text{)} \quad (3)$$

where  $k$  is the wavenumber in vacuum,  $C_1$  and  $C_2$  denote the stress-optical coefficients and  $C_1 - C_2 = 3.36 \times 10^{-5} \text{ mm}^2/\text{kg}$ ,  $\Delta$  is the relative difference in refractive index between core and cladding and  $\hat{\theta}_d$  (in unit of degree) denotes the rms deviation of the angle fluctuations in the side air holes.

As a rough estimation, we assume that  $l = 0.01$  m,  $\hat{\theta}_d = 0.2^\circ$ , fiber length  $L=1$  km and  $\Delta =0.4$  percent. The birefringence of our fiber is  $5 \times 10^{-5}$  at a wavelength of 1550 nm, so that the calculated  $(\hat{\Gamma})^2 = 0.66$  m<sup>-2</sup>,  $h = 6.4 \times 10^{-5}$  m<sup>-1</sup> and the crosstalk  $CT \equiv 10 \log \frac{P_x}{P_y} = 10 \log(2hL) = -9$  dB (the factor 2 comes from the round-trip of the signal along the fiber). This value indicates that the polarisation crosstalk remains tolerable over 1 km (less than 13% signal contamination by the orthogonal polarisation), but may turn critical over longer distances, in agreement with observations in classical polarisation-maintaining fibers showing similar birefringences.

It should be noted that the waveguide deformations are factors intrinsic to the sole fiber structure, setting a lower bound for the mode coupling. Extrinsic factors such as microbendings in real situations will also impact on the crosstalk, but integrating this aspect is beyond the scope of this study at this stage.

## 6. Conclusion

In summary, we propose a distributed pressure sensing based on  $\Phi$ -OTDR and a special fiber with elliptical core and 2 side air holes in the cladding. Thanks to the large air holes in the fiber, its birefringence is very sensitive to pressure changes, which translates into a frequency compensation of 159 MHz/bar, while the temperature sensitivity is kept at only 6 MHz/K. It is quite remarkable that this simple fiber structure can lead to such good responses, fully comparable with much more sophisticated photonic crystal designs, offering a very affordable solution to the lingering problem of distributed pressure sensing.

Owing to the high sensitivity of  $\Phi$ -OTDR, associated to the low transmission and splicing losses to standard fibers observed with this SAHF, long distance ( $\sim 720$  m) distributed pressure sensing is demonstrated with high spatial resolution (5 cm). The potential to further reduce the temperature sensitivity is discussed, which is verified through simulation and can be realized by changing the size and orientation of the core ellipse. The crosstalk between polarizations is discussed which can provide an estimation of the sensing length limitation of a given fiber.

**Funding.** TEAMTECH programme of the Foundation for Polish Science co-financed by the European Union under the European Regional Development Fund (NODUS); H2020 Marie Skłodowska-Curie Actions (FINESSE 722509).

**Acknowledgments.** The authors thank Dr. Jiangtao Zhou from EPFL for the kind help to obtain the SEM image of the fiber.

**Disclosures.** The authors declare no conflicts of interest.

**Data availability.** Data underlying the results presented in this paper are not publicly available at this time but may be obtained from the authors upon reasonable request.

## References

1. Y. Fu, R. Zhu, B. Han, H. Wu, Y.-J. Rao, C. Lu, and Z. Wang, "175-km Repeaterless BOTDA With Hybrid High-Order Random Fiber Laser Amplification," *J. Lightwave Technol.* **37**(18), 4680–4686 (2019).
2. A. Dominguez-Lopez, M. A. Soto, S. Martin-Lopez, L. Thévenaz, and M. González-Herráez, "Resolving 1 million sensing points in an optimized differential time-domain Brillouin sensor," *Opt. Lett.* **42**(10), 1903–1906 (2017).
3. D. Chen, Q. Liu, X. Fan, and Z. He, "Distributed Fiber-Optic Acoustic Sensor With Enhanced Response Bandwidth and High Signal-to-Noise Ratio," *J. Lightwave Technol.* **35**(10), 2037–2043 (2017).
4. L. Costa, H. F. Martins, S. Martín-López, M. R. Fernández-Ruiz, and M. González-Herráez, "Fully distributed optical fiber strain sensor with 10–12  $\epsilon/\sqrt{\text{Hz}}$  sensitivity," *J. Lightwave Technol.* **37**(18), 4487–4495 (2019).
5. X. Lu, P. J. Thomas, and J. O. Hellevang, "A Review of Methods for Fibre-Optic Distributed Chemical Sensing," *Sensors* **19**(13), 2876 (2019).
6. R. Magalhães, A. Garcia-Ruiz, H. F. Martins, J. Pereira, W. Margulis, S. Martin-Lopez, and M. Gonzalez-Herraez, "Fiber-based distributed bolometry," *Opt. Express* **27**(4), 4317–4328 (2019).
7. S. Liehr, M. Breithaupt, and K. Krebber, "Distributed Humidity Sensing in PMMA Optical Fibers at 500 nm and 650 nm Wavelengths," *Sensors* **17**(4), 738 (2017).
8. X. Bao and L. Chen, "Recent Progress in Distributed Fiber Optic Sensors," *Sensors* **12**(7), 8601–8639 (2012).
9. A. Barrias, J. R. Casas, and S. Villalba, "A Review of Distributed Optical Fiber Sensors for Civil Engineering Applications," *Sensors* **16**(5), 748 (2016).
10. A. Masoudi and T. P. Newson, "Contributed review: Distributed optical fibre dynamic strain sensing," *Rev. Sci. Instrum.* **87**(1), 011501 (2016).

11. L. Schenato, A. Galtarossa, A. Pasuto, and L. Palmieri, "Distributed optical fiber pressure sensors," *Opt. Fiber Technol.* **58**, 102239 (2020).
12. A. Méndez and E. Diatzikis, "Fiber optic distributed pressure sensor based on Brillouin scattering," in *Optical Fiber Sensors*, (Optical Society of America, 2006), p. ThE46.
13. G. Zhang, H. Gu, H. Dong, L. Li, and J. He, "Pressure sensitization of Brillouin frequency shift in optical fibers with double-layer polymer coatings," *IEEE Sens. J.* **13**(6), 2437–2441 (2013).
14. Y. Dong, L. Qiu, Y. Lu, L. Teng, B. Wang, and Z. Zhu, "Sensitivity-enhanced distributed hydrostatic pressure sensor based on BOTDA in single-mode fiber with double-layer polymer coatings," *J. Lightwave Technol.* **38**(8), 2564–2571 (2020).
15. Y. H. Kim, H. Kwon, J. Kim, and K. Y. Song, "Distributed measurement of hydrostatic pressure based on Brillouin dynamic grating in polarization maintaining fibers," *Opt. Express* **24**(19), 21399–21406 (2016).
16. L. Teng, H. Zhang, Y. Dong, D. Zhou, T. Jiang, W. Gao, Z. Lu, L. Chen, and X. Bao, "Temperature-compensated distributed hydrostatic pressure sensor with a thin-diameter polarization-maintaining photonic crystal fiber based on Brillouin dynamic gratings," *Opt. Lett.* **41**(18), 4413–4416 (2016).
17. T. Chen, Q. Wang, R. Chen, B. Zhang, C. Jewart, K. P. Chen, M. Maklad, and P. R. Swinehart, "Distributed high-temperature pressure sensing using air-hole microstructural fibers," *Opt. Lett.* **37**(6), 1064–1066 (2012).
18. R. M. Gerosa, J. H. Osório, D. Lopez-Cortes, C. M. Cordeiro, and C. J. De Matos, "Distributed pressure sensing using an embedded-core capillary fiber and optical frequency domain reflectometry," *IEEE Sens. J.* **21**(1), 360–365 (2021).
19. L. Schenato, A. Pasuto, A. Galtarossa, and L. Palmieri, "An optical fiber distributed pressure sensing cable with pa-sensitivity and enhanced spatial resolution," *IEEE Sens. J.* **20**(11), 5900–5908 (2020).
20. S. Mikhailov, L. Zhang, T. Geernaert, F. Berghmans, and L. Thévenaz, "Distributed Hydrostatic Pressure Measurement Using Phase-OTDR in a Highly Birefringent Photonic Crystal Fiber," *J. Lightwave Technol.* **37**(18), 4496–4500 (2019).
21. L. Zhang, L. D. Costa, Z. Yang, M. A. Soto, M. González-Herráez, and L. Thévenaz, "Analysis and Reduction of Large Errors in Rayleigh-Based Distributed Sensor," *J. Lightwave Technol.* **37**(18), 4710–4719 (2019).
22. Y. Koyamada, M. Imahama, K. Kubota, and K. Hogari, "Fiber-Optic Distributed Strain and Temperature Sensing With Very High Measurand Resolution Over Long Range Using Coherent OTDR," *J. Lightwave Technol.* **27**(9), 1142–1146 (2009).
23. H. M. Xie, K. Okamoto, P. Dabkiewicz, and R. Ulrich, "Side-hole fiber for fiber-optic pressure sensing," *Opt. Lett.* **11**(5), 333 (1986).
24. J. Clowes, S. Syngellakis, and M. Zervas, "Pressure sensitivity of side-hole optical fiber sensors," *IEEE Photonics Technol. Lett.* **10**(6), 857–859 (1998).
25. L. Zhang, Z. Yang, Ł. Szostkiewicz, K. Markiewicz, T. Nasilowski, and L. Thévenaz, "Fully distributed pressure sensing with ultra-high-sensitivity using side-hole fibers," in *Optical Fiber Sensors*, (Optical Society of America, 2018), p. WF13.
26. E. Chmielewska, W. Urbańczyk, and W. J. Bock, "Measurement of pressure and temperature sensitivities of a Bragg grating imprinted in a highly birefringent side-hole fiber," *Appl. Opt.* **42**(31), 6284 (2003).
27. X. Lu, M. A. Soto, and L. Thévenaz, "Temperature-strain discrimination in distributed optical fiber sensing using phase-sensitive optical time-domain reflectometry," *Opt. Express* **25**(14), 16059–16071 (2017).
28. G. B. Hocker, "Fiber-optic sensing of pressure and temperature," *Appl. Opt.* **18**(9), 1445–1448 (1979).
29. T. Martynkien, A. Anuszkiewicz, G. Statkiewicz-Barabach, J. Olszewski, G. Golojuch, M. Szczurowski, W. Urbanczyk, J. Wojcik, P. Mergo, M. Makara, T. Nasilowski, F. Berghmans, and H. Thienpont, "Birefringent photonic crystal fibers with zero polarimetric sensitivity to temperature," *Appl. Phys. B* **94**(4), 635–640 (2009).
30. K. Takada, K. Okamoto, Y. Sasaki, and J. Noda, "Ultimate limit of polarization cross talk in birefringent polarization-maintaining fibers," *J. Opt. Soc. Am. A* **3**(10), 1594–1603 (1986).
31. K. Okamoto, Y. Sasaki, and N. Shibata, "Mode coupling effects in stress-applied single polarization fibers," *IEEE J. Quantum Electron.* **18**(11), 1890–1899 (1982).